International Journal of Pharmaceutics 663 (2024) 124562

Contents lists available at ScienceDirect

International Journal of Pharmaceutics

journal homepage: www.elsevier.com/locate/ijpharm

From self-Assembly to healing: Engineering ultra-Small peptides into supramolecular hydrogels for controlled drug release

Marilisa Pia Dimmito [a], Lisa Marinelli [a,*], Ivana Cacciatore [a], Eleonora Chiara Toto [a], Barbara Albertini [b], Antonella Fontana [a,c], Serena Pilato [a], Marcella Reale [d], Erica Costantini [d], Cristiano Pesce [e], Antonio Di Stefano [a,c], Paolo Caliceti [e]

[a] University "G. d'Annunzio" of Chieti-Pescara, Department of Pharmacy, Via dei Vestini 31, 66100, Chieti, Italy
[b] Dompè Pharmaceutici S.p.A., Via Campo di Pile, s.n.c. 67100 L'Aquila (AQ), Italy
[c] UdA TechLab Center (UdATech), Via Dei Vestini 31, 66100 Chieti, Italy
[d] Department of Innovative Technologies in Medicine and Dentistry "G. d'Annunzio", Via dei Vestini 31, 66100 Chieti, Italy
[e] Department of Pharmaceutical and Pharmacological Sciences, University of Padova, Via F. Marzolo 5, 35131 Padova, Italy

ARTICLE INFO

Keywords:
Gastrointestinal diseases
Hydrogels
Lipopeptides
Self-assembling
Wound healing

ABSTRACT

The aim of this study was the evaluation of suitability of novel mucoadhesive hydrogel platforms for the delivery of therapeutics useful for the management of disorders related to the gastrointestinal tract (GI). At this purpose, here we describe the preparation, the physicochemical characterization and drug delivery behaviour of novel hydrogels, based on self-assembling lipopeptides (**MPD02-09**), obtained by covalently conjugating lauric acid (LA) to SNA's peptide derivatives gotten by variously combining D- and L- amino acid residues. LA conjugation was aimed at improving the stability of the precursor peptides, obtaining amphiphilic structures, and triggering the hydrogels formation through the self-assembling. Budesonide (**BUD**), an anti-inflammatory drug, was selected as model because of its use in the treatment in GI disorders. Preliminary studies were performed to correlate the chemical structure of the conjugates with the key physicochemical properties of the materials for drug delivery. Two lipopeptides, **MPD03** and **MPD08**, were found to form hydrogels (**MPD03h** and **MPD08h**, respectively) with characteristics suitable for drug delivery. These materials showed mucoadhesiveness of about 60 %. *In vitro* studies carried out with **BUD** loaded hydrogels showed about 70 % drug release within 6 h. Wound healing assessed in Caco-2 and HaCaT cells, showed reduction of cell-free area to values lower than 10 %. Taking together these results **MPD03h** and **MPD08h** have been shown to be excellent candidates for **BUD** delivery.

1. Introduction

Hydrogels can be defined as structures arranged into two- or three-dimensional network, possessing the capability to absorb substantial quantities of water or biological fluids. They can mimic natural tissues and have been applied in the biomedical field for the development of drug delivery systems (DDSs), in tissue regeneration, and wound healing (Buwalda et al., 2014, Marinelli et al., 2020). Hydrogels exhibiting proper rheological properties, are purposed in industrial and biomedical fields, since by applying mechanical stress or strain they can undergo gel-sol transition that immediately recovers back into gel upon stress removal (Chen et al., 2017). Among the applications, the wound healing is one of the most accredited (Guan et al., 2022). Hydrogel dressings with personalized designs, can offer advantages in wound treatment, encompassing haemostasis, infection and inflammatory response, angiogenesis, and re-epithelialization, well working in moist environments (Rudyardjo and Wijayanto, 2017). This water-absorbing capacity is primarily attributed to the hydrophilic moieties (*i.e.*, amide, amino, carboxyl, and hydroxyl groups) along the molecular chains of hydrogelators. The presence of these groups impacts on the hydrogels physicochemical properties, including porosity, structural softness, swelling capacity, and elasticity. Notably, these properties closely resemble those of biological systems, differentiating hydrogels from other synthetic biomaterials (Hanafy et al., 2019). The hydrogelators transform into larger elongated aggregates, creating entanglements that contribute to the formation of a network (Du et al., 2015), which may exhibit elastic properties or involve interactions between the nanostructures, resulting in a higher density of physical crosslinks, which promote the

* Corresponding author at: University "G. d'Annunzio" of Chieti-Pescara, Department of Pharmacy, Via dei Vestini 31, 66100, Chieti, Italy.
E-mail address: lisa.marinelli@unich.it (L. Marinelli).

https://doi.org/10.1016/j.ijpharm.2024.124562
Received 5 June 2024; Received in revised form 31 July 2024; Accepted 4 August 2024
Available online 5 August 2024

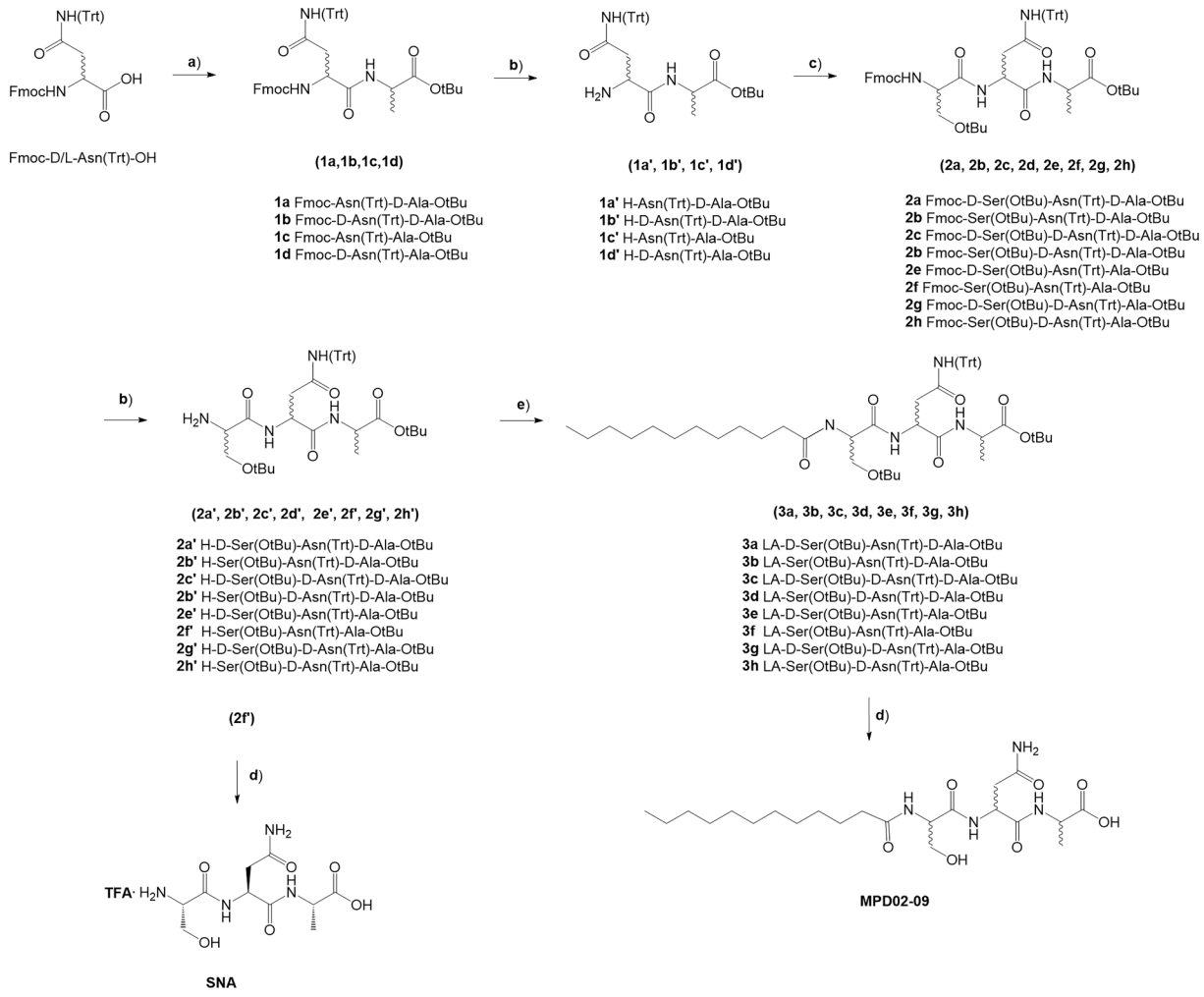

Scheme 1. Reagent and conditions: **a)** EDC·HCl (1.1 eq), HOBt anhydrous (1.1 eq), NMM (1.1 eq) DMF anhydrous, 0 °C; H-DAla-OtBu hydrochloride salt/H-Ala-OtBu hydrochloride salt, NMM (2.2.eq), r.t. overnight; **b**) piperidine 20 % DMF, 1 h, room temperature; **c**) Fmoc-DSer(OtBu)–OH/Fmoc-Ser(OtBu)–OH, DMF anhydrous, 0 °C, EDC·HCl (1.1 eq), HOBt anhydrous (1.1 eq), NMM (2.2.eq); **1a**'/**1b**'/**1c**'/**1d**', NMM (1.1 eq), r.t. overnight; **d**) TFA, overnight; **e**) lauric acid, EDC·HCl (1.1 eq), HOBt anhydrous (1.1 eq), NMM (1.1 eq), DMF anhydrous, 0 °C, **2a**'/ **2b**'/**2c**'/**2d**'/**2e**'/**2f**'/**2g**'/**2h**', NMM (1.1 eq), r.t. overnight.

nanostructure's bundling leading to gelation (Du et al., 2015). Typically, hydrogels are formed through molecular self-assembly (SA), a natural and free energy-driven process, that organizes molecules into stable, ordered, and well-defined structures, below the equilibrium through mutual noncovalent interactions (including dipole–dipole, π-π stacking, hydrogen-bonding, Van der Waals, hydrophobic, and electrostatic interactions), by easily modifying the assembling environment (pH, ionic strength, temperature, and solvents) (La Manna et al., 2021). This process represents a powerful tool in the fabrication of nano- and microstructures with tunable properties, holding significant potential for applications in the field of drug-delivery (DD) (Huang et al., 2019). Among the compounds possessing SA's properties, peptides have a quite important role; they are composed of amino acids – typically less than 50 – linked via amide bonds (Gupta et al., 2020), and offer advantages such as high and precise biological activity, low toxicity, and biodegradability, but they also face significant challenges as pharmaceuticals due to their limited oral bioavailability and low stability within the human body (Al Musaimi et al., 2022). Countless approaches have been reported to overcome these drawbacks to enhance their utility in the pharmaceutical field, particularly captivating for the creation of novel DDSs with proper drug release features and combining low systemic toxicity (Zhang and Bulaj, 2012, Mitrovic et al., 2023). Moreover, peptide structures are tuneable to be modified. More in detail, the peptide headgroups can be conjugated to hydrophobic tails of variable length, in most cases represented by alkyl chains, giving peptide amphiphiles (PAs). The hydrophobic tail increases the amphiphilicity of the molecule and drives its self-assembly in aqueous media, through the nanostructure's formation. PAs with single tail, often assemble into fibres with the hydrophobic tails packing in the core away from the solvent and the hydrophilic head facing the surface; in proper conditions, the nanofibers entangle into hydrogels (Paramonov et al., 2006).

PAs are attractive candidates as DDSs since the level of hydrophobicity may be proper modulated, influencing the absorption, distribution, metabolism, excretion, and bioavailability of entrapped active ingredients (Li et al., 2016a). Starting from these knowledges, we investigated the modification of an ultra-short peptide with the sequence Ser-Asn-Ala (**SNA**), previously reported to exert moderate antibacterial activity against both Gram-positive and –negative bacteria (Das and Das, 2021). To overcome the shortcomings related to the fast enzymatic degradation, physical and chemical instabilities, and short half-life, we addressed the lipidation of a series of **SNA**'s analogues obtained by covalently introducing the lauric acid (LA) and varying the combination of D- and L-amino acids. These strategies aim at enhancing the stability and obtain novel self-assembling lipopeptides, namely **MPD02-09**, capable of forming ordered supramolecular hydrogels with potential applications as platform for the DD also working as wound dressing materials. Moreover, we explored the suitability of these hydrogels by loading the budesonide (**BUD**) as prototype of anti-

inflammatory drug, commonly used in eosinophilic esophagitis and other pathological conditions, such as ulcerative colitis, characterized by inflammation and ulcers, associated with blood in stool and severe pain. In addition, the hydrogels were characterized in terms of Critical Gelation Concentration (CGC), surface tension, rheological properties, morphological features and mucin binding properties. Moreover, they were subjected to *in vitro* release studies as well as biological assays to assess the release profile, the cytotoxicity, and the applicability as wound dressing materials.

2. Experimental section

2.1. Materials

Acetonitrile (ACN), ethyl acetate (EtOAc), diethylether (Et_2O), dichloromethane (DCM), N,N-dimethylformammide (DMF), ethanol (EtOH), *n*-hexan, N-(3-dimethylaminopropyl)-N'-ethylcarbodiimide hydrochloride (EDC·HCl), hydroxybenzotriazole (HOBt), N-methylmorpholine (NMM), Mucine type II, budesonide, Dulbecco's Modified Eagle Medium (DMEM) supplemented with 10 % (*v/v*) FBS, 1 % (*v/v*) penicillin and 1 % (*v/v*) streptomycin and DMEM, supplemented with 2 mM L-glutamine, 100 U/mL streptomycin and 10 % heat-inactivated fetal bovine serum (FBS) were purchased from Merck KGaA, Darmstadt, Germany, Caco-2 cells were purchased from American Type Culture Collection (ATCC, Manassas, VA). Chromatographic columns purifications were performed on silica gel using column chromatography (Merck and co. 60, 230–400 mesh ASTM silica gel). NMR spectra were recorded with a Varian VXR-300 spectrometer (Varian Medical Systems, Inc., Paolo Alto, CA, USA). Human keratinocytes (HaCaT) cell lines from adult skin were purchased by Cell Line Service (CLS Eppelheim, Baden-Württemberg, Germany).

2.2. Peptide chemistry

SNA and **MPD02-09**, were synthesized using a standard solution-phase coupling/deprotection procedure outlined in the Scheme 1. In general, to a solution of Fmoc-Asn(Trt)–OH/Fmoc-D-Asn(Trt)–OH (1 eq) in DMF, at 0 °C, EDC·HCl (1.1 eq), HOBt anhydrous (1.1 eq), followed by NMM (1.1 eq) were added and mixed for 10 min. Subsequently, H-AlaOtBu/H-DAla-OtBu hydrochloride salt and NMM (1.1 eq) were added, and the mixture was stirred overnight at room temperature. After DMF removal, the crude mixture was extracted with EtOAc and washed three times with 5 % citric acid, $NaHCO_3$ss, and brine. The organic phase was collected, dehydrated using sodium sulfate, filtered, and dried (Minelli et al., 2012). The intermediates **1a**, **1b**, **1c**, **1d** were then purified by silica gel column (1:50, crude:silica ratio) using a mixture of DCM:EtOAc (8:2) and the pure compounds were obtained in high yields (90 %). Fmoc deprotection was achieved using a 20 % piperidine/DMF solution at room temperature for 1 h. After DMF removal, the crude mixture was extracted with EtOAc and washed three times with HCl (0.5 N). The organic phase was dried, and precipitated using *n*-hexane, to obtain the intermediates **1a'**, **1b'**, **1c'**, **1d'**, which were used for the subsequent steps without further purification.

Fmoc-Ser-(OtBu)–OH/Fmoc-DSer-(OtBu)–OH (1 eq) was dissolved in DMF at 0 °C, then EDC·HCl (1.1 eq), HOBt anhydrous (1.1 eq), and NMM (1.1 eq), were added and the mixture was stirred for 10 min at 0 °C. Subsequently, intermediate **1a'/1b'/1c'/1d'** was added, followed by NMM (1.1 eq) and stirred overnight at room temperature.

After DMF removal, the crude was suspended in EtOAc and washed three times with 5 % citric acid, $NaHCO_3$ss, and brine. The organic phase was collected and dried using sodium sulfate, filtered, and dried. The intermediates **2a**, **2b**, **2c**, **2d**, **2e**, **2f**, **2g**, and **2h** were monitored by TLC using DCM: EtOAc (8:2) and purified by silica gel column under the same eluent conditions (1)(1:70, crude:silica ratio). The intermediates were obtained in good yield (70 %).

Next, **2a**, **2b**, **2c**, **2d**, **2e**, **2f**, **2g**, **2h** were deprotected using a 20 % piperidine/DMF solution at room temperature for 1 h. The DMF was removed, and the residue taken-up with EtOAc and washed three times with HCl (0.5 N). The organic phase was collected and completely dried, leading to compounds **2a'**, **2b'**, **2c'**, **2d'**, **2e'**, **2f'**, **2g'**, **2h'**.

The intermediate **2f'** was treated with TFA for 2 h and precipitated in cold ether (three times) to get **SNA**.

To obtain **MPD02-09**, at a stirring solution containing LA (1 eq) in DMF at 0 °C, EDC·HCl (1.1 eq), HOBt anhydrous (1.1 eq), and NMM (1.1 eq) were added and mixed for 10 min at 0 °C. In the second reaction step, **2a'/2b'/2c'/2d'/2e'/ 2f'/2g'/2h'** were added, followed by NMM (1.1 eq), and stirred at room temperature overnight. After removing DMF, the residue was extracted with EtOAc and washed three times with 5 % citric acid, $NaHCO_3$ss, and brine. The organic phases were collected, dehydrated using sodium sulphate, filtered, and dried, giving the intermediates **3a**, **3b**, **3c**, **3d**, **3e**, **3f**, **3g**, **3h.** The latter were subjected to a final deprotection using TFA. After precipitation in cold ether, **MPD02-09** were obtained in good overall yield as white powders.

2.3. Hydrogels preparation

For unloaded hydrogels, the appropriate amount of **MPD02-09** was added in 150 mM phosphate buffer (PBS), pH 7.4, to reach 4- or 8-mM concentrations. The resulting mixture was heated to 80 ± 5 °C, under stirring, and left to stay for 5 min. The gelation was achieved after cooling down the solution to room temperature. For **BUD**-loaded hydrogels (**BUD-MPD03/08h**), the selected lipopeptides were dissolved in PBS, the solution was brought to 80 ± 5 °C and left to stay for 5 min. In the meantime, a stock solution of **BUD** (10 mg/mL) in EtOH was added to the hot lipopeptide dispersion to reach a final concentration of 250 μg/mL (0.6 mM). The gelation was achieved after cooling down to room temperature (Wang et al., 2019).

2.4. Critical gelation concentration (CGC), density and surface tension analysis

The Critical Gelation Concentration (CGC) was determined by heating to 80 ± 5 °C, 4- and 8-mM hydrogels, to obtain a clear liquid solution easily transferable in a glass vial for the lyophilization. Next, the lyophilized samples were resuspended by adding 100 μL of Milli-Q water, vortexed, heated in a water bath at 80 ± 5 °C, and cooled to room temperature to verify the gel formation. This procedure was repeated after several Milli-Q water aliquot addition, until reaching a concentration where the gel is no longer formed. Next, the density was calculated by weighing 1 mL of the obtained solutions. The surface tensions of **MPD02-09h** were calculated according to the pendant drop method as reported by Daerr and Mogne (Daerr and Mogne, 2016). Briefly, **MPD02-09h** sessile drops were made to fall from a hanged micropipette tip. The images were captured quickly as the drops were about to detach and were investigated using plugin drop analysis.

2.5. High performance liquid chromatography (HPLC) analysis of MPD03 and MPD08

The HPLC analysis were performed using an Agilent 1260 Infinity II HPLC (Agilent, Santa Clara, CA, USA) consisting of a 1260 Infinity II Quaternary Pump (model G7111A), 1260 Infinity II auto-sampler (model G7129A), a 1260 Infinity II Multicolumn Thermostat (model G7116A), and a 1260 Infinity II Diode Array Detector (model G7115A) equipped with a Poroshell 120 EC-C18 column (150 x 4.6 mm i.d., particle size 4 μm, Agilent, Santa Clara, USA) operating at 20 °C. The samples were analysed in a gradient elution mode using a mixture of Milli-Q water (A) and ACN (B), both enriched with 0.1 % of TFA, as follow: 5 % of B for 2 min, 5–100 % B from 2 to 16 min, 100 % of B from 16 to 18 min, 100–5 % of B from 18 to 20 min, 5 % from 20 to 22 min. The flow rate was 0.8 mL/min, with a UV detector set at 214 nm.

Table 1
Sequences of **SNA** and **MPD 02–09**.

Compound	Sequence
SNA	H-Ser-Asn-Ala-OH
MPD02	LA-Ser-Asn-Ala-OH
MPD03	LA-Ser-Asn-D-Ala-OH
MPD04	LA-Ser-D-Asn-Ala-OH
MPD05	LA-D-Ser-Asn-Ala-OH
MPD06	LA-Ser-D-Asn-D-Ala-OH
MPD07	LA-D-Ser-Asn-D-Ala-OH
MPD08	LA-D-Ser-D-Asn-Ala-OH
MPD09	LA-D-Ser-D-Asn-D-Ala-OH

2.6. In vitro proteolytic stability

Human plasma, obtained from 3H Biomedical (Uppsala, Sweden, Europe), was thawed and thermostated to 37 ± 0.5 °C. The peptides were dissolved in DMSO and individually poured in human plasma (90 % of plasma) until reaching 8 mM concentrations. At predefined time point, 100 µL of plasma samples were transferred into a 2 mL Eppendorf tube and a protein crash was performed using, as precipitation solvent, cold 0.01 M HCl in MeOH (200 µL). Next, the suspensions were vortexed and placed at 4 °C for 30 min and subjected to centrifugation at 14,000 g for 20 min. The collected supernatants were analysed by HPLC using the method described in section 2.5 for the quantification of the remaining % of **SNA**, **MPD03**, **MPD08** and LA. (Cornacchia et al., 2022).

2.7. Swelling and degradation studies

BUD-MPD03h and **BUD-MPD08h** (8 mM and 0.6 mM in terms of lipopeptides and **BUD**, respectively) were prepared in glass vials, as described in section 2.3. Next, 0.4 mL of PBS (150 mM, pH 7.4) was added to the gels and the vials were incubated at 37 ± 5 °C for 12 h. At predefined time intervals, the buffer was removed from the formulation surface, and the hydrogels were weighted to define the variations in terms of weight once in contact with aqueous environment. Data presented were obtained by the mean values of three independent measurements. The swelling ratio (SR) was calculated considering the ratio between the swollen and the initial hydrogel weight, according to the Eq. (1) (Wu et al., 2020):

$$SR = W_t/W_0 \quad (1)$$

where $\mathbf{W_t}$ is the swollen hydrogel weight and $\mathbf{W_0}$ is the initial hydrogel weight.

2.8. Rheological properties

Mechanical and rheological properties of **MPD02-09h** were evaluated using a modular compact rheometer MCR-102e (Anton

Table 2
Density, surface tension, gelation ability and critical gelation concentration (CGC) for **MPD02-09h** (4 and 8 mM).

Formulation	Concentration (mM)	Density (g/cm^3)	Surface Tension (mN/m)[a]	Gelation ability	CGC (mM)
MilliQ-Water	4	0.995	77.44 (±3.37)	–	–
MPD02h		0.985	64.33 (±4.64)	soft gel	3.40
MPD03h		0.992	61.25 (±2.42)	gel	3.70
MPD08h		1.005	67.26 (±2.33)	gel	3.10
MPD09h		1.003	67.72 (±1.91)	soft gel	3.40
MPD02h		0.971	43.70 (±2.76)	gel	2.90
MPD03h	8	0.993	61.55 (±1.62)	gel	3.70
MPD05h		0.990	56.33 (±2.21)	gel	5.40
MPD08h		0.980	51.17 (±5.02)	gel	3.10
MPD09h		0.832	42.21 (±1.91)	gel	3.40

[a] Values are expressed as the mean of three independent experiments.

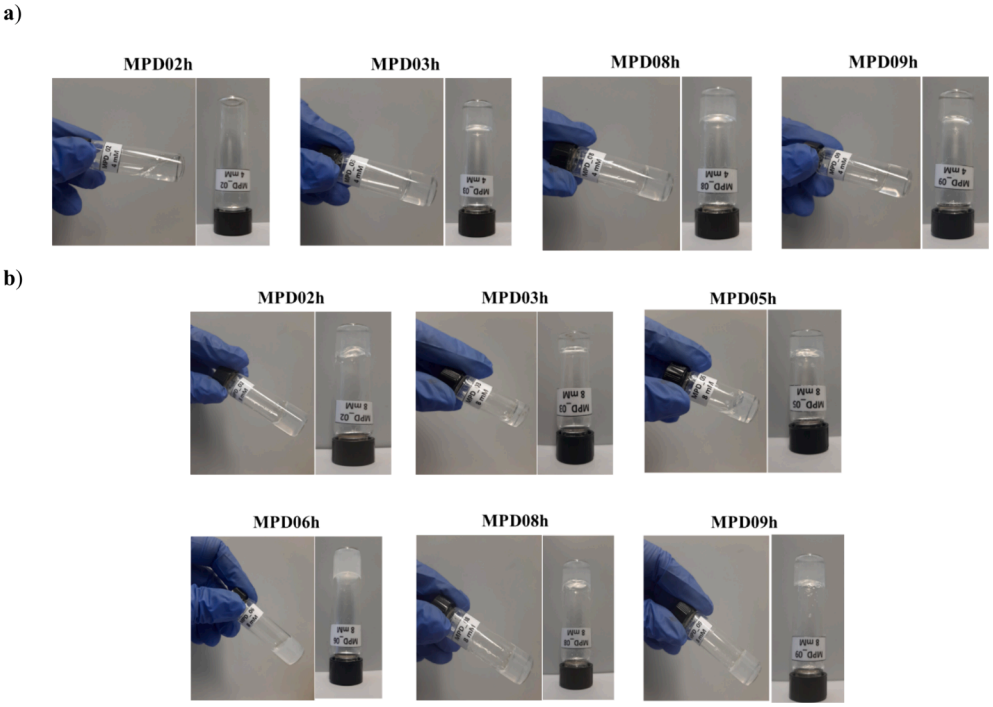

Fig. 1. Hydrogels prepared at concentration 4 mM **a)** and 8 mM **b)**.

Table 3
Plasma stability of **SNA**, **LA MPD03**, and **MPD08**.

SNA		LA		MPD03		MPD08	
$t_{1/2}$ (h)[a]	k_{obs} (h^{-1})[a]	$t_{1/2}$ (h)[a]	k_{obs} (h^{-1})[a]	$t_{1/2}$ (h)[a]	k_{obs} (h^{-1})[a]	$t_{1/2}$ (h)[a]	k_{obs} (h^{-1})[a]
1.543 (±0.37)	0.449 (±0.13)	> 24	–	12.08 (±0.37)	0.057 (±0.019)	13.78 (±0.42)	0.050 (±0.022)

[a] Values are expressed as the mean of three independent experiments.

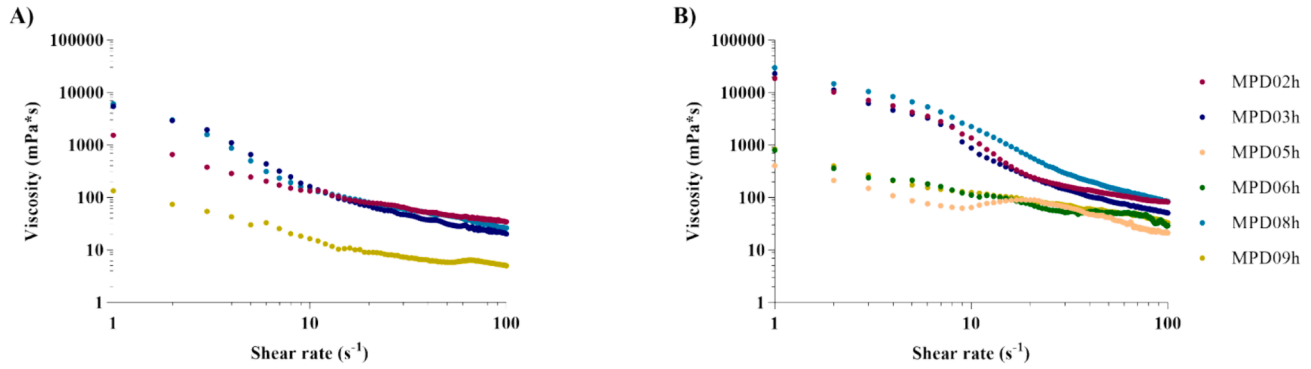

Fig. 2. Flow curves of **MPD02-09h** prepared at concentration 4 mM **a)** and 8 mM **b)**.

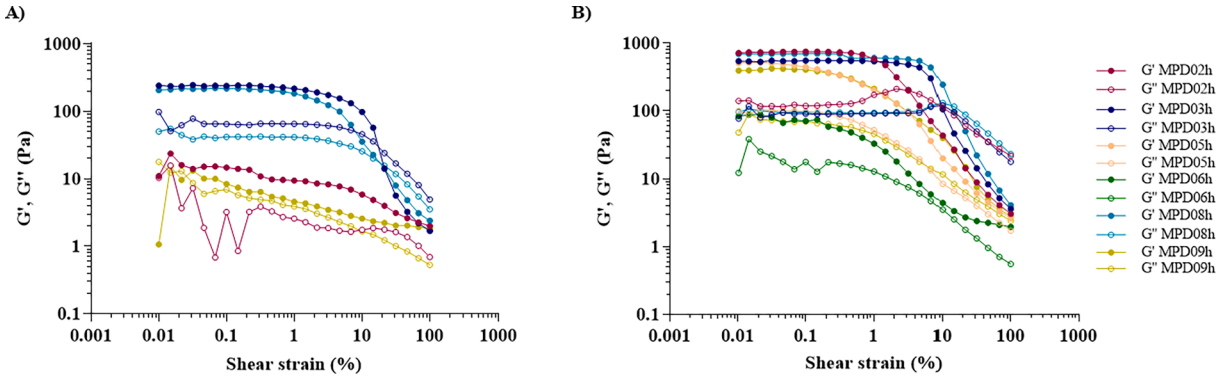

Fig. 3. Amplitude sweep tests of **MPD02-09h** prepared at concentration 4 mM **a)** and 8 mM **b)**.

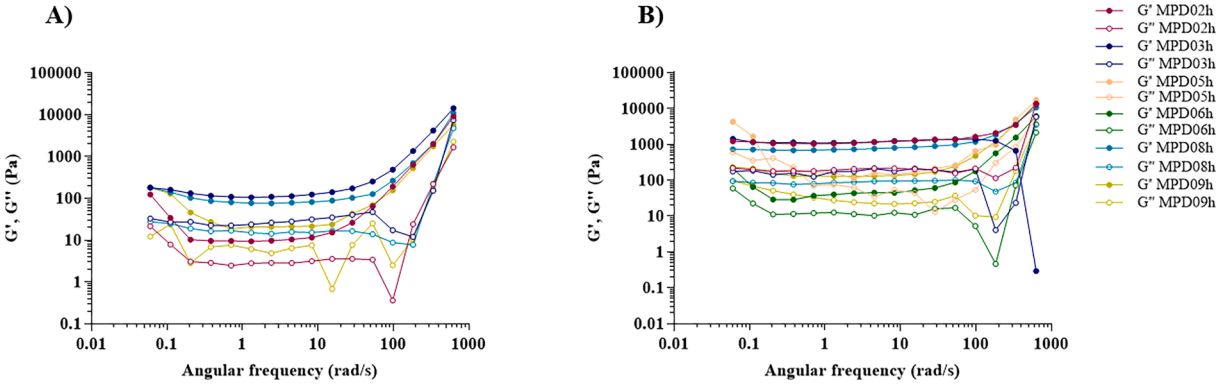

Fig. 4. Frequency sweep tests of **MPD02-09h** prepared at concentration 4 mM **a)** and 8 mM **b)**.

PaarCompass™) equipped with a measuring system PP25 SN80421. The hydrogels were transferred onto 25 mm parallel plate geometry, the gap height was adjusted to 1 mm and the temperature set at 25 °C. After the sample loading, the system was left to equilibrate for 5 min to reach thermal stability, and then analysed. The flow behaviour of hydrogels was investigated by measuring the viscosities as a function of the shear rates in the region of 1–100 s^{-1}. Oscillatory tests were carried out working in the frequencies range 0.06-628 rad/s , and setting a strain of 0.1 %, within the linear viscoelastic region (LVR), previously defined in amplitude stress sweep tests, where the material was subjected to shear strain percentage ranged from 0.01 to 100.

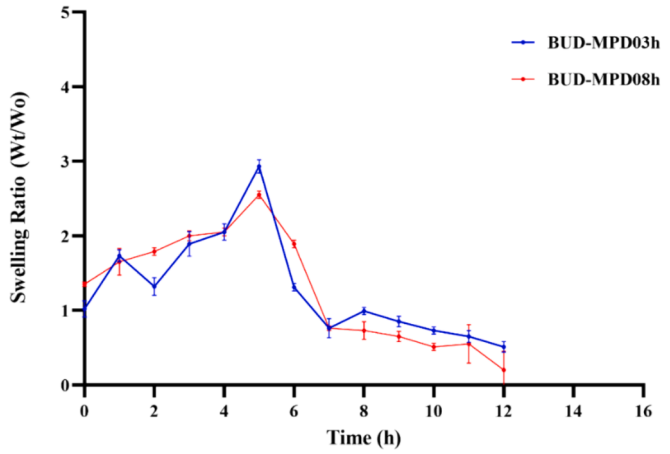

Fig. 5. **BUD-MPD03h** and **BUD-MPD08h** swelling ratio and degradation profile of hydrogels.

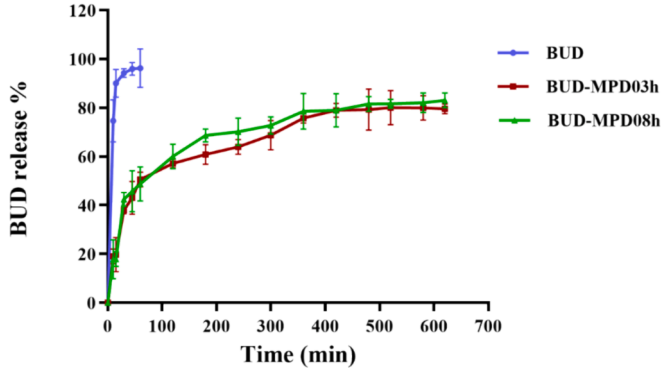

Fig. 6. **BUD** release from **MPD03h** and **MPD08h**.

2.9. Atomic force microscopy (AFM)

AFM images of the peptide-based hydrogels were captured by using MultiMode 8 AFM microscope with Nanoscope V controller (Bruker, Billerica, Massachusetts, US). **MPD02-09** solutions were prepared at a concentration of 0.06 mM (27 μg/mL) in EtOH and aliquots of 10 μL were placed on SiO_2 substrates followed by drying at room temperature overnight. The obtained samples were scanned by the silicon ScanAsyst-Air probe (triangular geometry, cantilever resonance frequency 70 kHz and nominal spring constant 0.4 N/m) in ScanAsyst in Air mode. Images of 512 x 512 pixels were collected with different scan sizes and the morphological analysis of the AFM data was performed using NanoScope Analysis 1.8 software.

2.10. Mucin-binding assay

Porcine mucin (PM) dissolved in PBS was incubated with 8 mM **MPD03h** and **MPD08h** at room temperature (25 ± 5 °C) for 2 h (1:1 *v/v*), before centrifugation for 60 min at 14,000 rpm and 4 °C. The remaining free PM in the supernatant was measured by UV spectrometry, setting the detector at 251 nm. The standard curve was determined using 50–350 μg/mL PM solution. The mucin adhesiveness was expressed as PM binding efficiency (BE %) calculated by the Eq. (2) (Wang et al., 2021):

$$BE\% = (C_0 - C_s)/C_0 \times 100 \quad (2)$$

where $\mathbf{C_0}$ is the initial concentration of PM used for incubation (400 μg/mL) and $\mathbf{C_s}$ is the concentration of free PM in the supernatant after the removal of **MPD03h** and **MPD08h**.

2.11. BUD release from hydrogels

Release studies were performed under conditions mimicking the GI tract (Ben Khalifa et al., 2022, D'Aurizio et al. 2011). In detail, **BUD-MPD03h** and **BUD-MPD08h** (5 mL) and the free **BUD**, at a drug concentration of 0.6 mM, were kept in contact with 50 mL of hydrochloric acid buffer (pH 1.5) for 2 h, then immersed 50 mL of PBS (pH 7.4) for 12 h. Both receiving solutions were enriched with 20 % of EtOH, to ensure the complete solubilization of **BUD**, and kept under stirring (250 rpm) at 37 ± 5 °C. At fixed time points, aliquots (100 μL) were withdrawn and replaced with fresh medium (Pandey et al., 2021). The concentration of **BUD** was detected by HPLC using the equipment described in section 2.5, in gradient elution mode by using 20 mM NaH_2PO_4 pH 3 (A) and ACN (+0.1 % TFA), as follows: 90 % of A (0–1 min), 10 % of A (1–6 min), 10 % of B (6–8 min), 90 % of A (8–10 min). The results were obtained as percentage of cumulative release over time using the Eq. (3) (Marinelli et al., 2024).

$$Cumulative\ drug\ release\% = \left(\frac{Volume\ of\ sample\ withdrawn\ (mL)}{Bath\ volume}\right) * P(t-1) + Pt \quad (3)$$

where $\mathbf{P_t}$ and $\mathbf{P_{(t-1)}}$ are percentages released at time t and before t, respectively .

2.12. Cell cultures

Caco-2 cell line derived from human Colorectal Adenocarcinoma was used as a model of human intestinal epithelial cells. Caco-2 cells were cultured in DMEM supplemented with 10 % (*v/v*) FBS, 1 % (*v/v*) penicillin and 1 % (*v/v*) streptomycin at 37 ℃ in a humidified 5 % CO_2 atmosphere. When the cells were about 80 % confluent, they were subcultured and differentiated by replacing the medium every 2 days, for fourteen days, according to Geirnaert *et al.* (Geirnaert et al. 2017).

HaCaT cell line derived from human keratinocytes was employed as a model of epidermal keratinocytes. The cells were cultured at the density of 0.2 × 10^6 cell/cm^2 in plastic tissue culture flasks in DMEM. Cells were maintained at 37 °C in a 95 % air humidified atmosphere and 5 % CO_2 in a Hera Cell 150 (Heraeus) incubator. After reaching the 90 % confluence, the cells were trypsinized and plated for further experiments.

2.13. Cell viability assay

To evaluate the effects of **SNA**, **MPD02-09**, **BUD-MPD03h** and **BUD-MPD08h** on cell viability, according to different experimental requirements, 100 μL/well of cell suspension were placed in 96 well plates (Caco-2 cells 0.16 × 10^6 cell/well, HaCaT cells 0.2 × 10^6 cell/well). After culture, cells were carefully rinsed with PBS and added of fresh medium conditioned with different concentrations (0.002, 0.02 and 0.2 mM) of selected compounds and formulations for 24 h. Cells cultured in the presence of growth medium alone, were used as the control.

Then the MTT assay was performed to analyze the effect of **MPD02-09h**, **BUD-MPD03h** and **BUD-MPD08h**, on both Caco-2 and HaCaT cells viability. At the end of the incubation, the culturing medium was discarded, and MTT reagent was added at a concentration of 5 mg/mL. After 2 h of incubation with MTT reagent, formazan was dissolved in DMSO and the absorbance was detected at 570 nm using GloMax-Multi detection System (Promega, Madison, WI, USA). The results expressed in O.D. units, were compared to untreated cells and reported as percentage of control (%) according to the Eq. (4):

$$\%CellViability = (O.D._{570}treatedcells) \times 100/(O.D._{570}control) \quad (4)$$

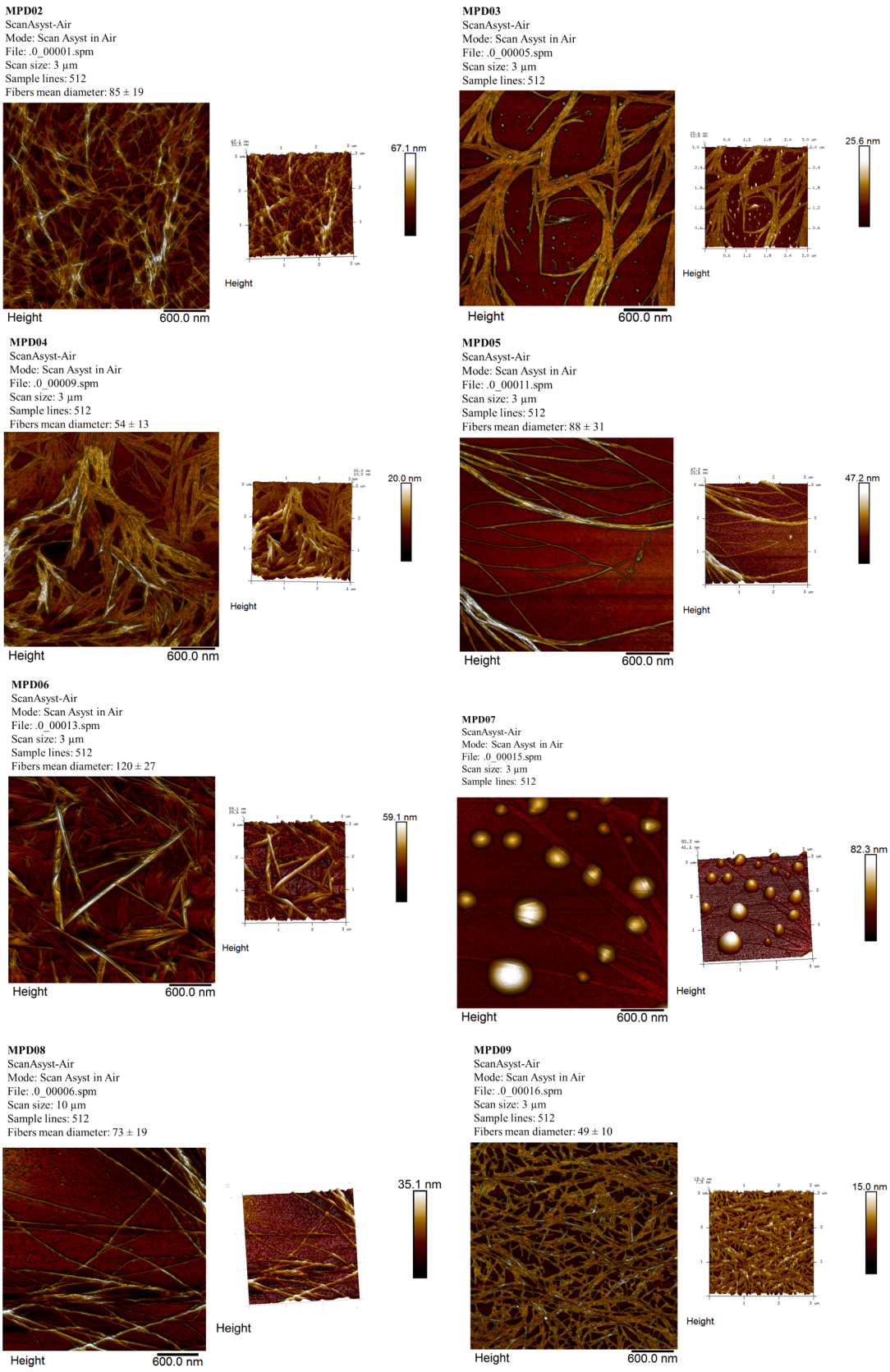

Fig. 7. Atomic force microscopy images of developed **MPD02-09**.

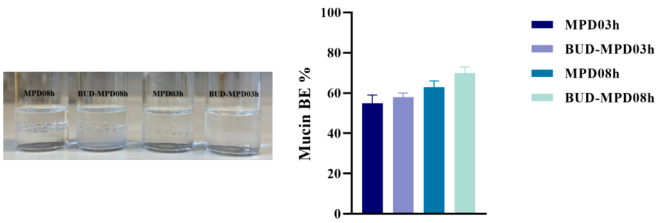

Fig. 8. Mucin binding assay of **MPD03h**, **BUD-MPD03h**, **MPD08h**, and **BUD-MPD08h**.

2.14. Wound healing

Wounds were generated in different sets of experiments for two different cell lines (Caco-2 and HaCaT). Caco-2 cells were seeded at a concentration of 0.6 × 10^6 cells/well cultured in a 12-well plate and differentiated for 14 days changing the medium every two days. Similarly, HaCaT cells were seeded at a density of 0.8 × 10^6 cells/well in a 12-well plate with or without 0.002, 0.02 and 0.2 mM of different compounds and incubated at 37 °C in a 5 % CO_2 (*v/v*) humidified incubator. When cells reached about 90 % confluence, were serum-starved overnight, and the monolayer of synchronized cells was gently scratched across the centre of the well with a sterile pipette tip (Ø = 0.1 mm). After scratching, debris were removed by washing with PBS and fresh medium, containing 0.002, 0.02 and 0.2 mM of **SNA**, **MPD02-09**, or 0.002, 0.02 and 0.2 mM **BUD-MPD03h**, **BUD-MPD08h**, and **BUD** was added till the wound closure. Untreated scratched cells represented the control.

2.15. Wound healing images acquisition

To follow the growth characteristics, the "wounded" area was photographed immediately after wounding and at specific time points, (0,

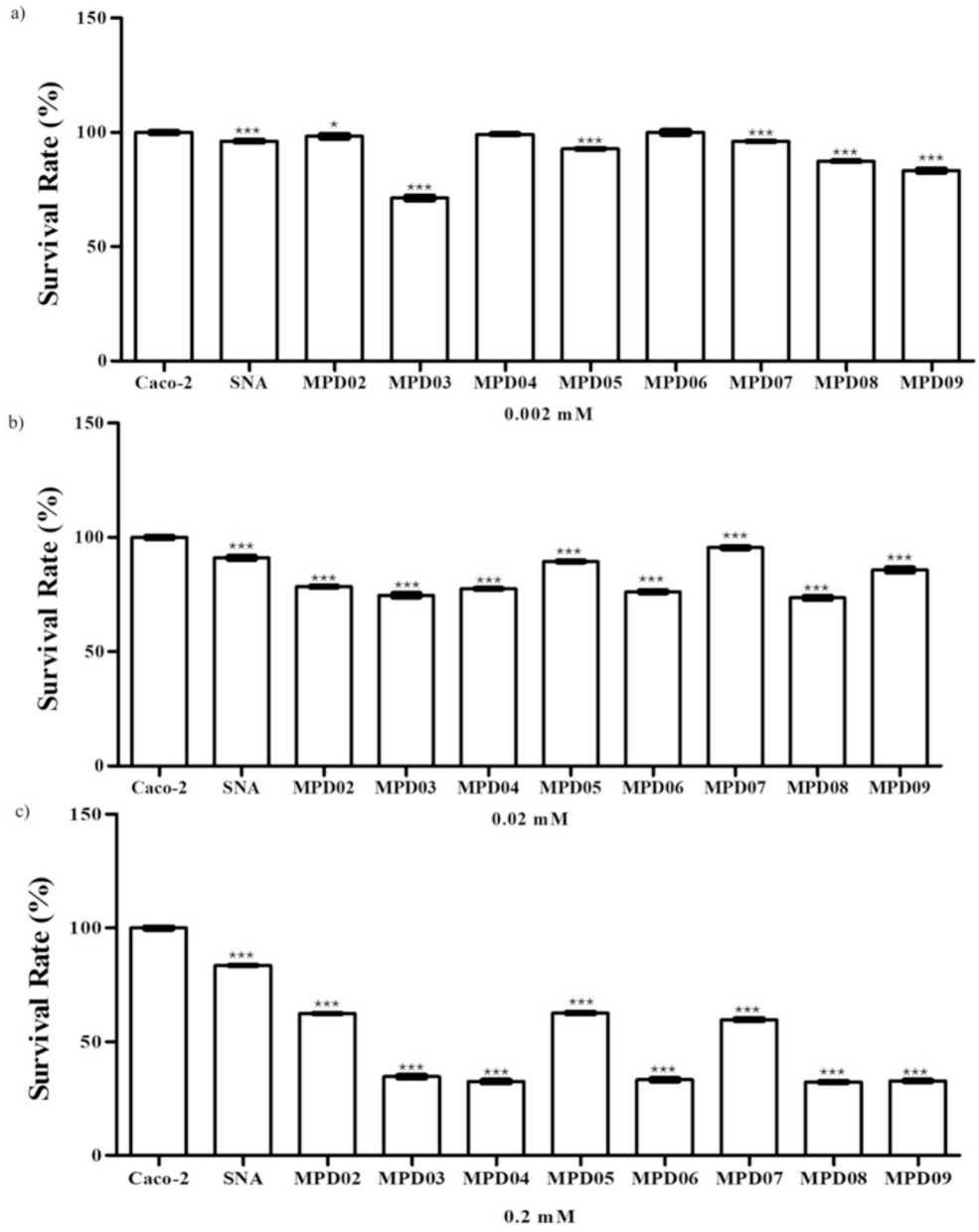

Fig. 9. Caco-2 cell viability. Cell survival rate assessed after 24 h in presence of 0.2, 0.02, and 0.002 mM **SNA**, **MPD02-09**. Data are reported as mean percentage (%) of three independent experiments. Statistical difference between compounds *vs* untreated cells were *p < 0.05 and ***p < 0.001.

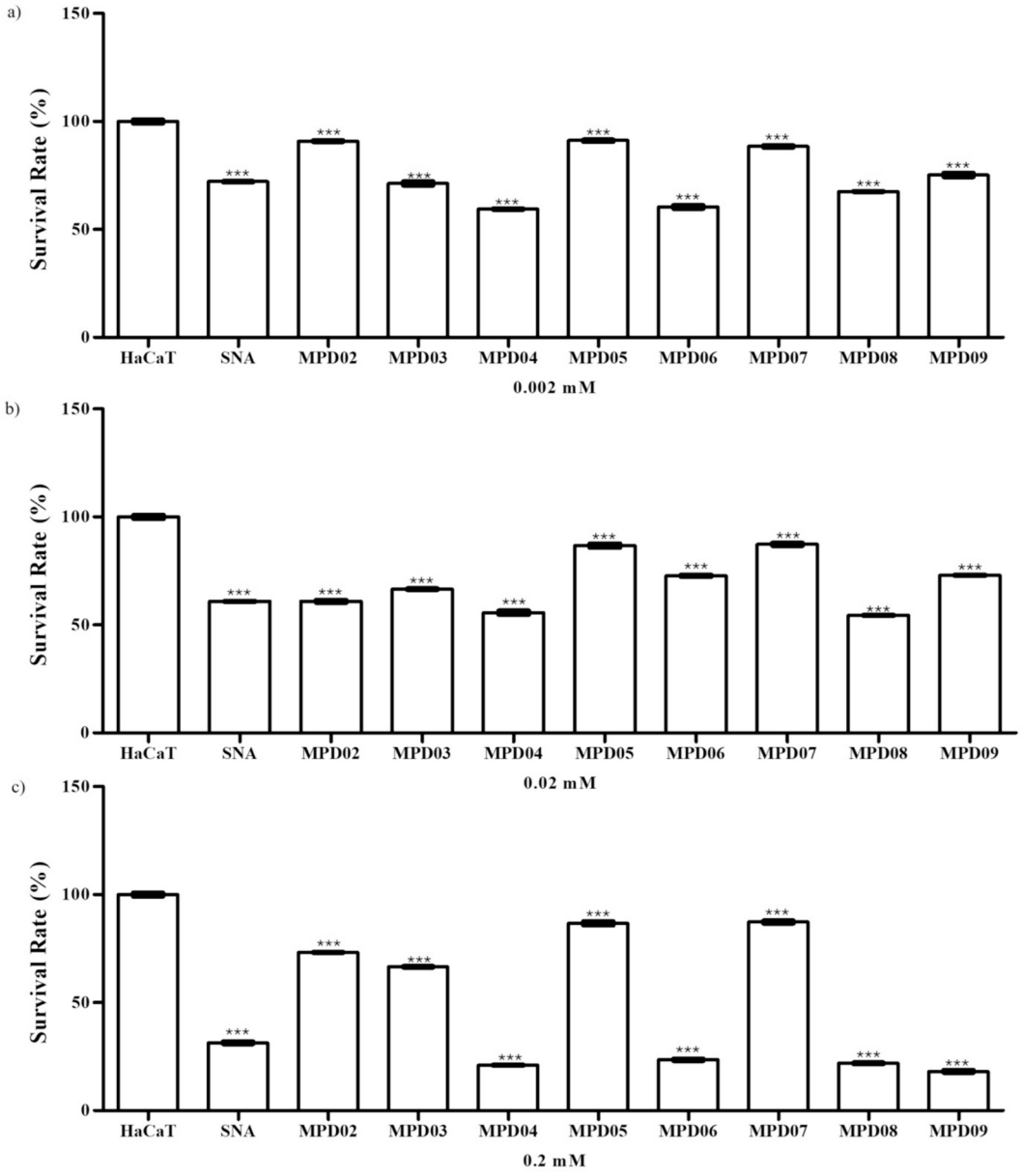

Fig. 10. HaCaT cell viability. Cell survival rate assessed after 24 h in presence of 0.2, 0.02, and 0.002 mM **SNA**, **MPD02-09**. Data are reported as mean percentage (%) of three independent experiments. Statistical difference between compounds *vs* untreated cells is ***$p < 0.001$.

18, 24, 48 and 72 h for Caco-2; 0, 6, 18 and 24 h for HaCaT) using an inverted light phase contrast microscope (Leica DMi1, Leica Microsystems, Germany) integrated with a digital camera (Leica MC120 HD, 2.5 M pixel, Leica Microsystems, Germany). NIH ImageJ software was used to process the images and to calculate the wound area dimension based on the perimeter (Schneider et al., 2012). Data were obtained from three independent experiments.

2.16. Statistical analysis

All experiments were repeated at least three times. GraphPad Software Inc. was used to analyse the data. Measurements were expressed as the mean ± SD or as percentage. Differences among multiple groups were compared using Kruskal-Wallis test. Differences between pairs of groups were assessed using Dunn's test for nonparametric pairwise multiple-comparison. The differences were considered significant at the $p < 0.05$.

3. Result and discussion

3.1. Hydrogelator design

In order to correlate the structure of lipopeptides with their physicochemical features for the production of hydrogels, a library of conjugates has been synthesised by conjugating LA to Ser-Asn-Ala tripeptides with different chiral structures.

Given the widely recognized procedure of peptides lipidation to obtain hydrogelators (Kurtzhals et al., 2023), it's likely that the gel properties of the selected lipopeptides are conferred by LA covalently conjugated to the tripeptide's backbone, as indicated by SNA's inability to gel under the same experimental conditions. The hydrophobic alkyl tail of LA imparts proper forces to the peptides, triggering self-assembly into nanostructures. Our findings support those reported by Wang et al., regarding the lipidated derivative of the YSV peptide, which, when conjugated with palmitic acid, resulted in nanostructures with superior aggregation properties (Wang et al., 2019). Table 1 reports the structure

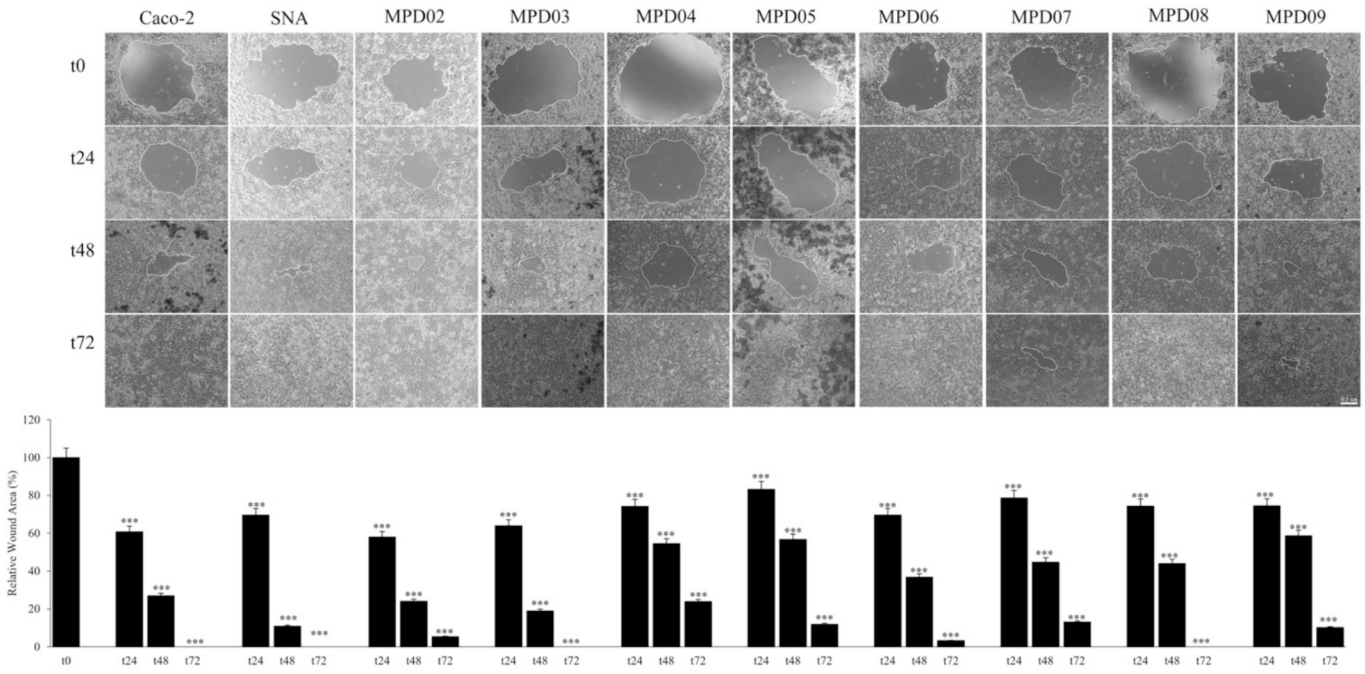

Fig. 11. Microscopy images of Caco-2 cells wound closure. The area of the wound was analyzed by phase-contrast microscopy and Image J software. Black lines indicate the leading edge of the wound, quantified at 0, 24, 48, and 72 h. In the images, the marked central cell-free area is surrounded by a low-density area. Columns represent the wound healing as a percentage (100 %) of the original (t0) area of the circular wound, measured in pixels. Data are reported as mean of three independent experiments. Statistical difference between compounds at different time point *vs* t0 (100 %) cells is ***$p < 0.001$.

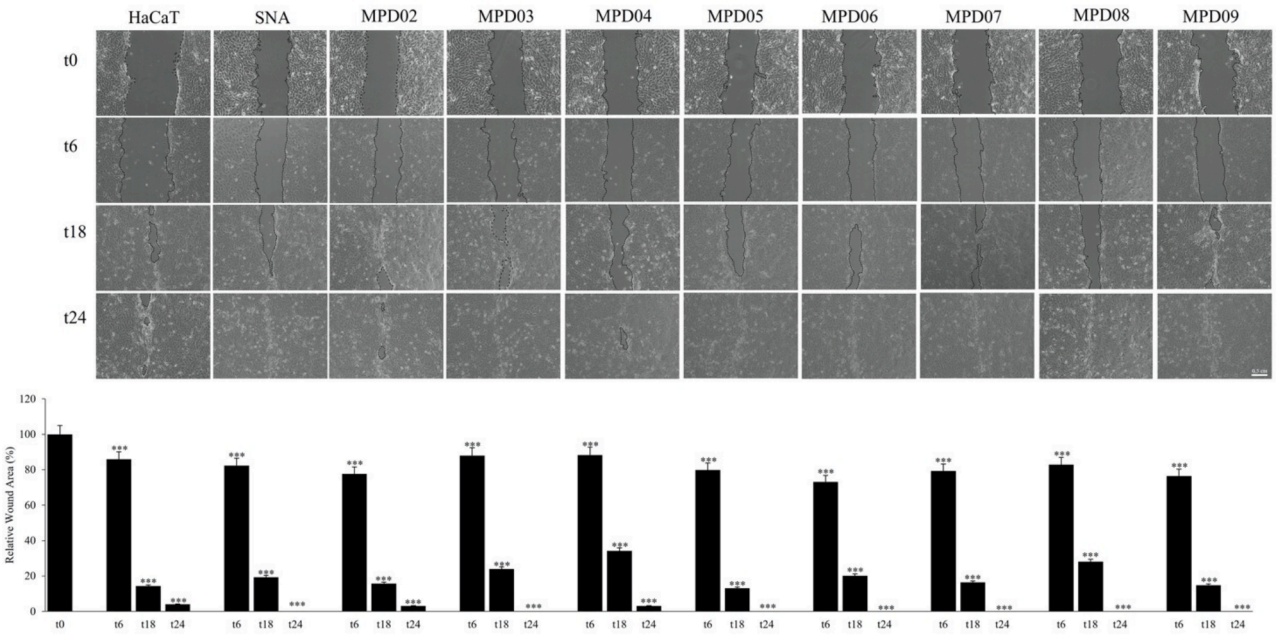

Fig. 12. Microscopy images of HaCaT cells wound closure. The area of the wound was analyzed by phase-contrast microscopy and Image J software. Black lines indicate the leading edge of the wound, quantified at 0, 6, 18, and 24 h. In the images, the marked central cell-free area is surrounded by a low-density area. Columns represent the wound healing as a percentage (100 %) of the original (t0) area of the scratch wound, measured in pixels. Data are reported as mean of three independent experiments. Statistical difference between compounds at different time point *vs* t0 (100 %) cells is ***$p < 0.001$.

of the synthesised lipopeptides, and Scheme 1 describes the synthetic procedure. After the synthesis, the lipopeptides were characterized in terms of ^{1}HNMR and ^{13}CNMR (see supporting information).

As previously described by Castelletto and colleagues, about the self-assembly of the lipopeptide C_{16}-KTTβAH as a promising hydrogel candidate with therapeutic potential for the breast cancer (Castelletto et al., 2019), in our study, we chosen LA for its carboxylic portion, facilitating the conjugation with SNA's *N*-terminus, enabling the tripeptide to form non-polar interactions such as Van der Waals and hydrophobic interactions, crucial for secondary assembly (Nitbani et al., 2022). Moreover, LA conjugated to peptide backbone, was reported to form nanofiber scaffolds capable of triggering angiogenesis, with

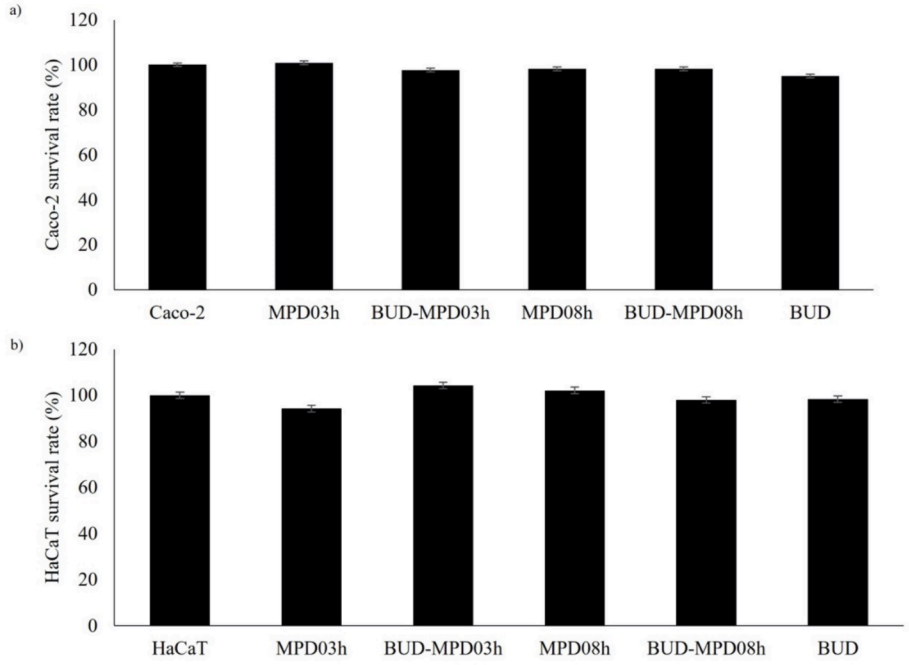

Fig. 13. Cell survival rate assessed after 24 h in untreated cells and treated with 0.002 mM of **BUD-MPD03h**, **MPD03h**, **BUD-MPD08h** and **MPD08h**, and **BUD**. Data are reported as mean percentage (%) of three independent experiments.

potential applications in thermal burn treatment (Yergoz et al., 2017).

MPD02-09 were designed to exploit the hydrogen-bond donor and acceptor properties of the amide and carbonyl groups of the peptide backbone, and the amide group in the Asn side chain, which are known to improve solubility in the aqueous environment (Roy et al., 2020). On the other side the methyl group of Ala, along with the alkyl tail of LA, may enhance hydrophobic interactions. The combination of these characteristics may yield assemblies, leading to nanofiber formation, which, under appropriate conditions, aggregate into dense networks providing the hydrogels formation.

3.2. Critical gelation concentration (CGC), density and surface tension analysis

The tendency of **MPD02-09** to self-assemble, was evaluated by estimation of the critical gelation concentration, while the hydrogel density and surface tension were estimated using the pendant drop method. Gelation studies showed that, **MPD02**, **MPD03**, **MPD08**, and **MPD09** undergo gelation at a concentration of 4 mM, while **MPD05**, **MPD06** showed a gelation point at 8 mM (Fig. 1). **MPD04** and **MPD07** were not able to gel even at high concentrations (20 mM).

Results revealed density comparable with that of water in the range 0.832–1.005 g/cm^3, while the found surface tensions, in all cases, were lower than that of water, ranging from 42.21 to 77.44 mN/m (Table 2). Notably, the variation in densities, of **MPD02-09h**, translates in more compact arrangement of hydrogelators chains (Tsutsumi et al., 2021). Similarly, the changes in surface tension values reflect variations in the surface interactions within the hydrogel network.

3.3. In vitro proteolytic stability

In plasma, considered as the worst case in terms of stability environment, **MPD03** and **MPD08** showed stability higher than that of **SNA** (Table 3), confirming the lipidation as a highly investigated approach, useful to improve the stability profile of peptides (Menacho-Melgar et al., 2019). However the stability remains lower than that of LA alone. Our findings confirm what previously reported for several peptide drugs, such as liraglutide, semaglutide, insulin degludec, and glucagon-like peptide 1, that exhibited advantageous and prolonged plasma stability when conjugated with $C_{14/16/18}$ fatty acids (Li et al., 2016b, Myšková et al., 2023).

3.4. Rheology

The rheological characterization started with flow curves, performed in the range of shear rates of 1–100 s^{-1}. Results highlight viscosities ranging from 10,000 to 10 mPa × s (Fig. 2), values normally recognized higher compared to that one of saliva, the first physiological medium with which the formulation will interact. Similarly, to saliva, which is recognized as a shear-thinning, non-Newtonian fluid, all the examined samples exhibited a typical shear-thinning behaviour, with their relative viscosities decreasing nearly linearly with shear rate, except for the range of lowest shear rate values (Rereddy et al., 2023).

These findings highlight the advantageous mechanical properties of the hydrogels, indicating a strong capacity to withstand stress and damage during the transit from the mouth to the stomach. The mechanical properties of novel developed hydrogels, were additionally assessed through oscillatory tests, crucial for determining their suitability for the intended biological applications. Particularly, the rigidity enables the hydrogels to maintain structural integrity, functioning as scaffolds, while mechanical stiffness could be essential for promoting cell adhesion.

Moreover, it is well known that the rheological properties can be useful to define the cohesiveness and the swallowing capability as well as mechanism-based drug release (Ong et al., 2018, Marcinkowska-Gapińska et al., 2018, Stojkov et al., 2021, Yan and Pochan, 2010).

In the oscillation mode, the strain sweep test, or amplitude sweep (Fig. 3), was preliminarily performed to identify the linear viscoelastic region (LVR), and to assess the storage (G') and loss (G'') moduli, two parameters describing the viscoelastic properties and the energy storage and dissipation, respectively. All the hydrogels revealed a linear viscoelastic behaviour, reflecting their capacity to predominantly maintain elasticity, within a wide range of strain amplitudes applied. Their G' exceeds the G'' within the LVR, suggesting strong mechanical integrity and stiffness, while the existence of a crossover point implies a potential transition to more viscous behaviour under heightened deformation. In

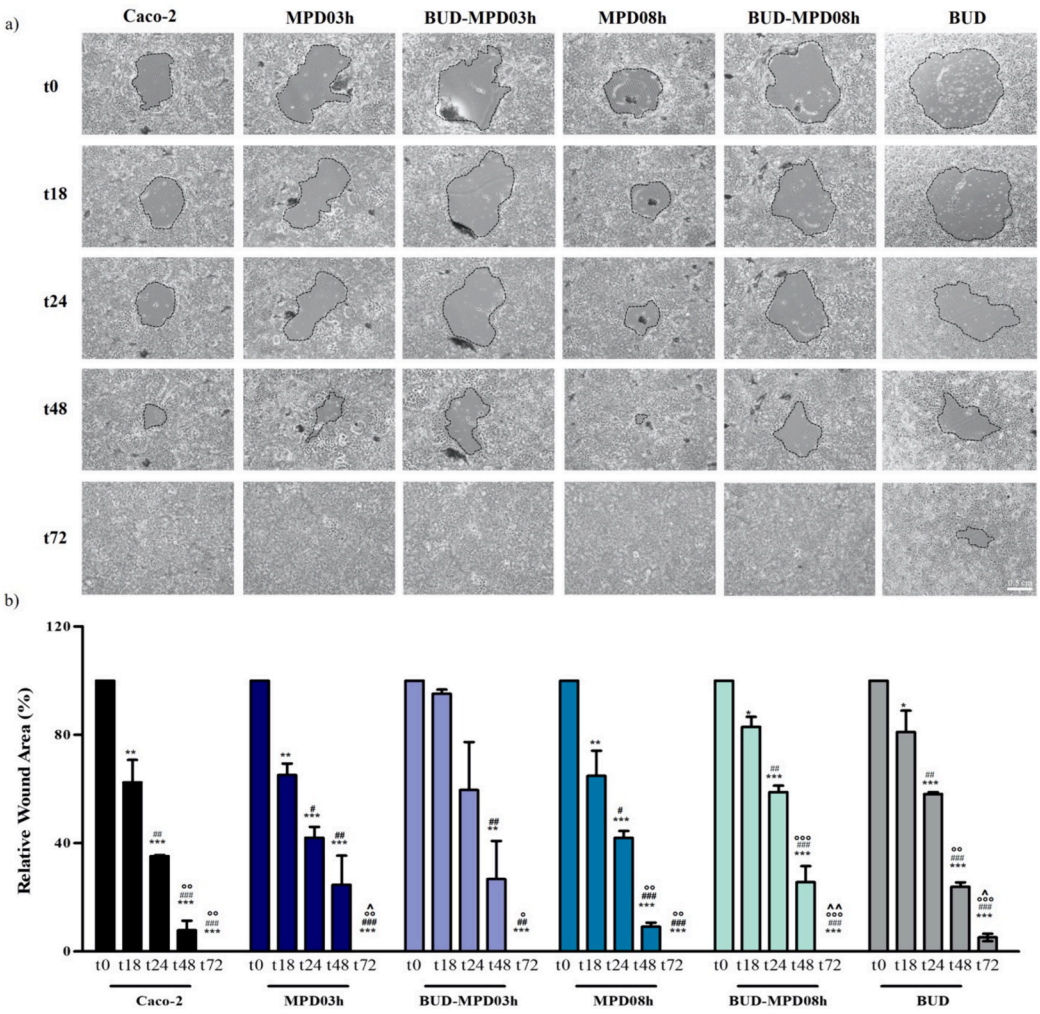

Fig. 14. A) microscopy images of caco-2 cells wound closure. The area of the wound was analyzed by phase-contrast microscopy and Image J software. Black lines indicate the leading edge of the wound, quantified at 0, 18, 24, 48, and 72 h. b) Bar graph represents the wound healing as a percentage of the original (t0) area of the circular wound, measured in pixels. In the images, the marked central cell-free area is surrounded by a low-density area. Data are reported as mean of three independent experiments. Statistical difference between each compounds at t18, t24, t48 and t72 *vs* t0 is ***p < 0.001, **p < 0.01. Statistical difference between each compounds at t24, and t48 *vs* t18 is ###p < 0.001, ##p < 0.01 and # p < 0.05. Statistical difference between each compounds at t48 and t72 *vs* t24 is °°°p < 0.001, °°p < 0.01 and °p < 0.05. Statistical difference between each compounds at t72 *vs* t48 is^^p < 0.01 and^p < 0.05.

contrast, **MPD05h**, **MPD06h**, and **MPD09h** consistently exhibit a higher G' than G'' throughout their amplitude sweep tests, without encountering a crossover point. Furthermore, the simultaneous decrease of both G' and G'' without a crossover point suggests that these hydrogels can deform resiliently, maintaining mechanical stability over a broad range of deformation conditions. The absence of a crossover point, combined with a shorter LVR, may indicate limitations in the material's tunability resulting in potentially unpredictable mechanical responses, complicating the accurate prediction of the material's behaviour under various loading conditions. Literature data suggest a correlation between the fiber content and the mechanical responsiveness of hydrogel materials. Starting from these evidence, rheological results were combined with those regarding the morphology, assessed by AFM. Indeed, it is well known that higher fiber content results in a shorter LVR region and a distinct crossover point, while lowest fiber amount outcome in an absence of the crossover point. **MPD08h** and **MPD05h** having the higher and lowest fiber content, respectively, reflect this behaviour. **MPD02-09h** based on 4–8 mM lipopeptides, were analysed by oscillation frequency tests at a constant strain of 0.1 % (Fig. 4). As showed in the figure with the increasing in concentration, both G' and G'' moduli increase. For all the tested samples G' was bigger than G'' within the range of considered frequencies, reaching 10 Pa for **MPD06h**, 100 Pa for **MPD05h**, and **MPD09h**, and 1,000 Pa for **MPD02h**, **MPD03h**, **MPD08h**. These values decrease in 4 mM hydrogels, showing a typical weak gel behaviour, with G' values of 100 Pa for **MPD03h** and **MPD08h** and 10 for **MPD02h** and **MPD09h**. An hydrogel intended for oral delivery should resist to deformation subsequent to peristaltic movements. Viscoelastic properties of **MPD03h** and **MPD08h**, suggest their proper resistance to deformation which translates into platforms with appropriate characteristics that make them suitable for intended oral administration (Budai et al., 2023, Stojkov et al., 2021).

3.5. Swelling and degradation studies

MPD03h and **MPD08h** showed similar degradation profiles. Swelling and degradation studies depict a significant degradation of the hydrogel after approximately 7 h of incubation, under physiological conditions at 37 ± 5 °C, with a maximum SR value of approximately 3 within 5 h (see Fig. 5). These results are in accordance with those of release studies, since after the first hour, the gel starts to swell, increasing its water content and allowing the diffusion of the loaded **BUD** into the receiving buffer, reaching the maximum SR within 5 h (Casadidio et al., 2018).

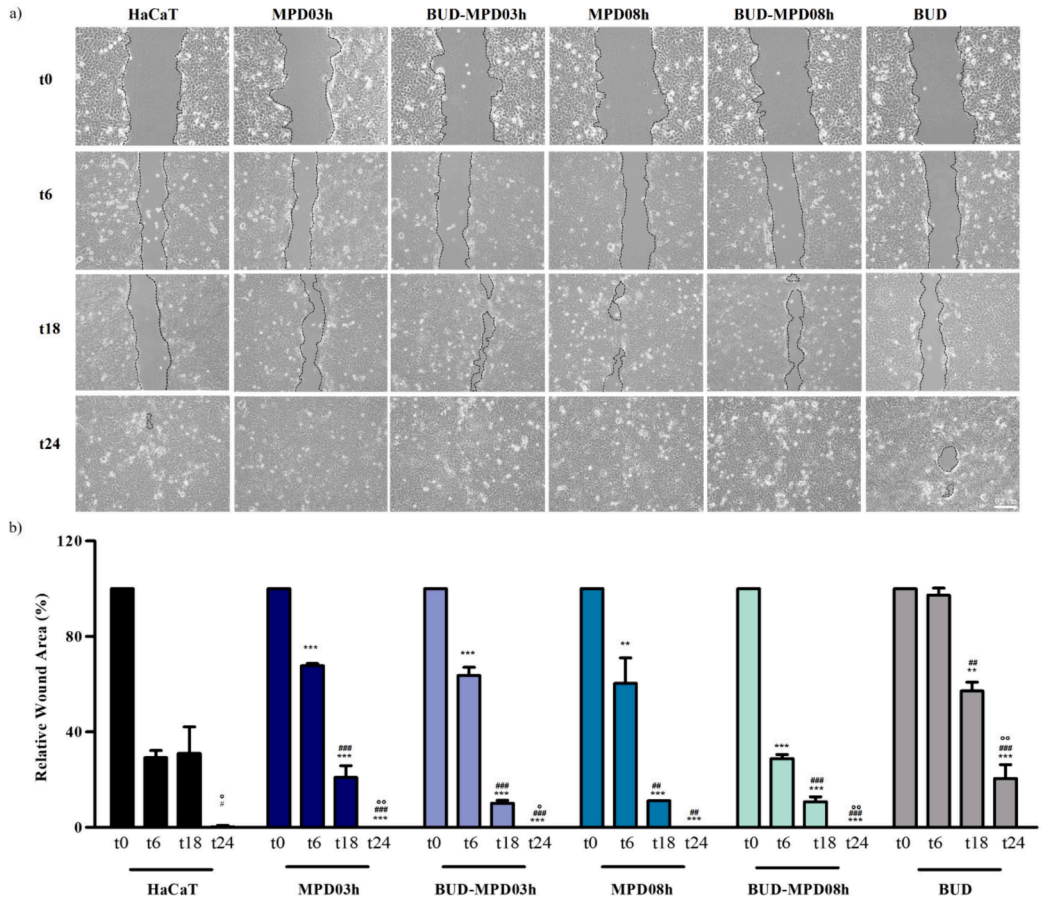

Fig. 15. A) microscopy images of hacat cells wound closure. the area of the wound was analyzed by phase-contrast microscopy and image j software. black lines indicate the leading edge of the wound, quantified at 0, 18, 24, 48, and 72 h. b) Bar graph represents the wound healing as a percentage of the original (t0) area of the wound, measured in pixels. In the images, the marked central cell-free area is surrounded by a low-density area. Data are reported as mean of three independent experiments. Statistical difference between each compounds at t18, t24, t48 and t72 *vs* t0 is ***p < 0.001, **p < 0.01. Statistical difference between each compounds at t24, t48 and t72 *vs* t18 is ###p < 0.001, ##p < 0.01 and #p < 0.05. Statistical difference between each compounds at t48 and t72 *vs* t24 is °°°p < 0.001, °°p < 0.01 and °p < 0.05. Statistical difference between each compounds at t72 *vs* t48 is^^p < 0.01 and^p < 0.05.

3.6. In vitro BUD release from MPD03h and MPD08h

By integrating biological and rheological properties, revealing suitable viscoelasticity as well as wound healing capacity, **MPD03** and **MPD08** emerged as the most effective hydrogelators, for this they were selected for delivery purposes. Aimed at exploring these materials for production of DDSs for oral delivery of anti-inflammatory drugs, hydrogels based on **MPD03** and **MPD08** (**MPD03h** and **MPD08h,** respectively) were loaded with **BUD**. The *in vitro* release profile from **MPD03h** and **MPD08h** resulted deeply dependent from their swelling ability into the dissolution media, as well as on the interaction between the drug and the lipopeptide fibrillar network. The release patterns (Fig. 6) were estimated in conditions mimicking the pHs and the transit time in the GI tract, in hydrochloric acid buffer and PBS at pHs of 1.5 and 7.4, respectively. The **BUD** release patterns from both hydrogels were overlappable and characterized by an initial burst release that provides about the 40 % of **BUD** release in 30 min, due to the presence of the drug on the hydrogel surface, followed by a more sustained release over the subsequent incubation time, probably depending on the drug entrapped into the fibrillar network. Initially, the rapid release was observed because the concentration gradient functioned as the driving force for the release. Subsequently, the release rate decreased as the drug near the surface was depleted. Graham and McNeil proposed that hydrogel's network allows the formation of permeation channels containing water for the diffusion of the entrapped drugs (Pandey et al., 2021).

3.7. Atomic force microscopy (AFM)

Atomic Force Microscopy (AFM) was employed to analyze the morphology of the self-assemblies formed by **MPD02-09**. The results (Fig. 7) revealed that **MPD02-09** self-assembles into fiber-like structures characterized by diverse morphologies and lengths, with diameters ranging from 49 to 120 nm. **MPD03** and **MPD08** exhibited longer fibers, contributing to a more rigid network. Specifically, **MPD08** showed a dense network composed of thin fibers homogeneously dispersed, whereas **MPD03** presented a high density of fibers closely associated with each other, leading to sections of highly dense fibers and regions devoid of them. Despite these differences in morphologies, there was no discernible impact on the mechanical properties, as both hydrogels exhibited similar responses to stress, as discussed in the rheological section. **MPD07** displayed a different morphology compared to other hydrogels, resembling that of nanoparticles. These findings highlight how alterations in amino acid chirality and/or their combination, can impact the overall morphology of the hydrogelators, emphasizing the role of molecular structure in dictating self-assembly behaviour (Hartgerink et al., 2001, Rani et al., 2016).

3.8. Mucin binding assay

Mucin binding assay was performed to explore the mucoadhesive properties of **MPD03h**, **BUD-MPD03h**, **MPD08h**, and **BUD-MPD08h**. The mucoadhesive properties are quite important for oral delivery

formulations, to withstand peristaltic movements as well as the washing effect of body fluids, that reduce the % of drug payload available systemically (Matthew et al., 2021). Mucoadhesive DDs can interact with the mucus layer covering the mucosal epithelial surface, increase the residence time of the dosage form at the absorption site (Silva et al., 2017). The drugs which have local action or those which have maximum absorption in GI tract require increased duration of stay at target level. Thus, mucoadhesive dosage forms are advantageous in increasing the drug plasma concentrations and therapeutic activity.

As showed in the Fig. 8 all **MPD03h**, **BUD-MPD03h**, **MPD08h**, and **BUD-MPD08h** possess high mucin binding efficiency, with **BUD-MPD08h** showing the highest value (75.1 ± 5.0 %). When comparing the **BUD**-loaded with the unloaded hydrogels, the results reveal slightly higher values for those formulations containing **BUD**, suggesting its possible involvement in improving the mucin binding affinity.

3.9. Cell viability of SNA and MPD02-09

Cell viability of **SNA** and **MPD02-09**, was assessed on Caco-2 and HaCaT cells after 24 h of incubation. The compounds were tested at 0.2, 0.02, and 0.002 mM, and cell viability was evaluated through MTT assay. Quantification of MTT after 24 h of treatment with varying doses of **SNA** and **MPD02-09** showed a dose-dependent loss of cell viability under each condition, although in a not significant way for both Caco-2 and HaCaT cells. The MTT assay showed that with 0.002 mM of **SNA** and **MPD02-09**, compared to the untreated control, cytotoxicity resulted less than 30 %, leading to the selection of this concentration for the following experiments (Figs. 9-10). These results are in agreement with those assessed by Lai *et al.* regarding the cell viability of lipidated peptides (Lai et al., 2022).

3.10. Wound healing of SNA and MPD02-09

Caco-2 cells were treated with 0.002 mM of **SNA**, **MPD02-09**, to investigate the healing properties. The circular wound areas were measured at different time points (t0, t24, t48 and t72) and the mean data of three independent experiments were reported in Fig. 11. Although all the tested compounds resulted able to significantly reduce the size of the cell-free area after 24–48 and 72 h, **SNA**, **MPD03** and **MPD08** resulted the most effective in induce a complete wound closure after 72 h of incubation (Motsoene et al., 2023).

Moreover, the healing properties of 0.002 mM of **SNA** and **MPD02-09** were investigated on HaCaT cells. The wounds areas were measured at different time points (t0, t18, t24 and t48). Cells migration was clearly visible on each side of the wound, which is marked with black lines. A significant reduction in the size of the cell-free area, measured by the distance between the edges of the scratch, was observed for **SNA**, **MPD 02–09** which can completely close the wounded area after 24 h, in comparison with the respective t0 size (100 % of cell-free area) (Fig. 12).

3.11. Viability of BUD-MPD03h, BUD-MPD08h, MPD03h and MPD08h

Considering the results of MTT assays as well as rheological tests, **MPD03h** and **MPD08h** were selected for the loading with **BUD**. **BUD-MPD03h, BUD-MPD08h, MPD03h** and **MPD08h** were prepared at 4 mM concentration in terms of hydrogelators and 0.6 mM (250 μg/mL) of **BUD**. Next, they were diluted to 0.002 mM and were subjected to investigation regarding the cell viability on both Caco-2 and HaCaT cell lines. After 24 h of treatment, no significant variation in cell survival rate was observed in both cell lines, as reported in Fig. 13.

3.12. Wound healing capability of BUD-MPD03h, BUD-MPD08h, MPD03h and MPD08h

Cell-free area of Caco-2 cells exposed to 0.002 mM of **BUD-MPD03h**, **BUD-MPD08h**, and **MPD03h** and **MPD08h**, for 72 h, showed a significant overtime reduction, as showed in Fig. 14.

Untreated and treated cells showed a complete wound closure after 72 h, in comparison with the gap size at t0 (100 %). The treatment with **BUD** alone does not allow the closure of the wound. Differences were observed for **MPD08h** that show the best efficacy already after 48 h, with a reduction of cell-free area from 100 % at t0 to 9 %. No significant differences were observed between the treatments.

24 h after the scratch, the treatment with **BUD-MPD03h**, **BUD-MPD08h**, and unloaded **MPD03h** and **MPD08h** significantly improved the rate of the monolayer repair process in HaCaT cells, compared to the t0 cell-free area. Unloaded **MPD03h** alone or in association with **BUD** showed a reduction of wound width from 100 % up to 17 % and 9 % respectively (Fig. 15). Similarly, **MPD08h** and **BUD-MPD08h** showed reduction in gap size with an 11 % and 7 %. No significant differences were observed between treatments.

4. Conclusion

In summary, hydrogels formulated with novel lipopeptides **MPD02-09** were proposed as a mucoadhesive platforms for the oral delivery of active compounds. Among the investigated formulations, **MPD03h** and **MPD08h** were identified as the most promising candidates for delivering **BUD**, selected as representative hydrophobic and anti-inflammatory drug. **MPD03h** and **MPD08h** facilitated approximately 70 % release of **BUD** within 5 h and possessed mucoadhesive properties, suggesting their potential application as oral viscous media for delivering **BUD** and other drugs. Moreover, the mucoadhesive properties displayed by loaded and unloaded **MPD03h** and **MPD08h**, are quite important for oral delivery formulations, since they allow to withstand peristalsis movements as well as the washing effect of body fluids, that reduce the % of drug payload available systemically, providing a certain oral viscous media suitable for applications in ulcerative colitis and eosinophilic esophagitis. Biological assays demonstrated that these formulations were non-cytotoxic according to the MTT test. Additionally, they exhibited significant potential in promoting wound closure, reducing the percentage of cell-free area in both Caco-2 and HaCaT cell monolayer assays. **MPD08h** showed wound healing properties after 48 h, reducing the cell-free area from 100 % to 9 % in the Caco-2 cell model. Similarly, **MPD03h**, either alone or in combination with **BUD**, led to substantial reductions in wound width on HaCat cell lines, ranging from 100 % to 17 % and 9 %, respectively. Likewise, unloaded **MPD08h**, both alone and in combination with **BUD**, demonstrated reductions in gap size of 11 % and 7 %, respectively. Further investigations in *in vivo* animal models are warranted to assess their effective suitability for the purposed application.

CRediT authorship contribution statement

Marilisa Pia Dimmito: Writing – review & editing, Writing – original draft, Investigation, Funding acquisition. **Lisa Marinelli:** Writing – review & editing, Writing – original draft. **Ivana Cacciatore:** Supervision, Conceptualization. **Eleonora Chiara Toto:** Investigation. **Barbara Albertini:** Investigation. **Antonella Fontana:** Methodology, Investigation. **Serena Pilato:** Investigation. **Marcella Reale:** Methodology, Investigation. **Erica Costantini:** Investigation. **Cristiano Pesce:** Investigation. **Antonio Di Stefano:** Supervision, Resources, Project administration, Methodology. **Paolo Caliceti:** Supervision, Methodology.

Declaration of competing interest

The authors declare that they have no known competing financial interests or personal relationships that could have appeared to influence the work reported in this paper.

Data availability

No data was used for the research described in the article.

Acknowledgments

This study was supported by Italian Ministry of Education, University and Research (University of Chieti-Pescara) FAR 2021.

Appendix A. Supplementary material

Supplementary data to this article can be found online at https://doi.org/10.1016/j.ijpharm.2024.124562.

References

Al Musaimi, O., Lombardi, L., Williams, D.R., Albericio, F., 2022. Strategies for improving peptide stability and delivery. Pharmaceuticals (Basel) 15, 1283.
Ben Khalifa, R., Cacciatore, I., Dimmito, M.P., Ciulla, M., Grande, R., Puca, V., Robuffo, I., De Laurenzi, V., Chekir-Ghedira, L., Di Stefano, A., Marinelli, L., 2022. Multiple lipid nanoparticles as antimicrobial drug delivery systems. J. Drug Deliv. Sci. Technol. 67, 102887.
Budai, L., Budai, M., Fülöpné Pápay, Z.E., Vilimi, Z., Antal, I., 2023. Rheological considerations of pharmaceutical formulations: focus on viscoelasticity. Gels 9, 469.
Buwalda, S.J., Boere, K.W., Dijkstra, P.J., Feijen, J., Vermonden, T., Hennink, W.E., 2014. Hydrogels in a historical perspective: from simple networks to smart materials. J. Control. Release 190, 254–273.
Casadidio, C., Butini, M.E., Trampuz, A., Di Luca, M., Censi, R., Di Martino, P., 2018. Daptomycin-loaded biodegradable thermosensitive hydrogels enhance drug stability and foster bactericidal activity against Staphylococcus aureus. Eur. J. Pharm. Biopharm. 130, 260–271.
Castelletto, V., Edwards-Gayle, C.J.C., Greco, F., Hamley, I.W., Seitsonen, J., Ruokolainen, J., 2019. Self-Assembly, tunable hydrogel properties, and selective anti-cancer activity of a carnosine-derived lipidated peptide. ACS Appl. Mater. Interfaces 11, 33573–33580.
Chen, M.H., Wang, L.L., Chung, J.J., Kim, Y.H., Atluri, P., Burdick, J.A., 2017. Methods to assess shear-thinning hydrogels for application as injectable biomaterials. ACS Biomater Sci. Eng. 3, 3146–3160.
Cornacchia, C., Marinelli, L., Di Rienzo, A., Dimmito, M.P., Serra, F., Di Biase, G., De Filippis, B., Turkez, H., Mardinoglu, A., Bellezza, I., Di Stefano, A., Cacciatore, I., 2022. Development of l-Dopa-containing diketopiperazines as blood-brain barrier shuttle. Eur. J. Med. Chem. 243, 114746.
D'Aurizio, E., Sozio, P., Cerasa, L.S., Vacca, M., Brunetti, L., Orlando, G., Chiavaroli, A., Kok, R.J., Hennink, W.E., Di Stefano, A., 2011. Biodegradable microspheres loaded with an anti-Parkinson prodrug: An in vivo pharmacokinetic study. Mol. Pharm. 8, 2408–2415.
Daerr, A., Mogne, A. 2016. Plugin to Measure the Surface Tension from an Image of a Pendent Drop, 62503945.
Das, S., Das, D., 2021. Rational design of peptide-based smart hydrogels for therapeutic applications. Front. Chem. 9, 770102.
Du, X., Zhou, J., Shi, J., Xu, B., 2015. Supramolecular hydrogelators and hydrogels: from soft matter to molecular biomaterials. Chem. Rev. 115, 13165–13307.
Geirnaert, A., Calatayud, M., Grootaert, C., Laukens, D., Devriese, S., Smagghe, G., De Vos, M., Boon, N., Van de Wiele, T., 2017. Butyrate-producing bacteria supplemented in vitro to Crohn's disease patient microbiota increased butyrate production and enhanced intestinal epithelial barrier integrity. Sci. Rep. 7, 11450.
Guan, T., Li, J., Chen, C., Liu, Y., 2022. Self-assembling peptide-based hydrogels for wound tissue repair. Adv. Sci. (weinh) 9, e2104165.
Gupta, S., Singh, I., Sharma, A.K., Kumar, P., 2020. Ultrashort peptide self-assembly: front-runners to transport drug and gene cargos. Front. Bioeng. Biotechnol. 29 (8), 504.
Hanafy, N.A.N., Leporatti, S., El-Kemary, M.A., 2019. Mucoadhesive hydrogel nanoparticles as smart biomedical drug delivery system. Appl. Sci. 9, 825.
Hartgerink, J.D., Beniash, E., Stupp, S.I., 2001. Self-assembly and mineralization of peptide-amphiphile nanofibers. Science 294, 1684–1688.
Huang, H., Qi, X., Chen, Y., Wu, Z., 2019. Thermo-sensitive hydrogels for delivering biotherapeutic molecules: a review. S.P.J. 7, 990–999.
Kurtzhals, P., Østergaard, S., Nishimura, E., Kjeldsen, T., 2023. Derivatization with fatty acids in peptide and protein drug discovery. Nat. Rev. Drug Discov. 22, 59–80.
La Manna, S., Di Natale, C., Onesto, V., Marasco, D., 2021. Self-assembling peptides: from design to biomedical applications. Int. J. Mol. Sci. 22, 12662.
Lai, Z., Chen, H., Yuan, X., Tian, J., Dong, N., Feng, X., Shan, A., 2022. Designing double-site lipidated peptide amphiphiles as potent antimicrobial biomaterials to combat multidrug-resistant bacteria. Front. Microbiol. 13, 1074359.
Li, Y., Wang, F., Cui, H., 2016a. Peptide-based supramolecular hydrogels for delivery of biologics. Bioeng. Transl. Med. 1, 306–322.
Li, Y., Wang, Y., Wei, Q., Zheng, X., Tang, L., Kong, D., Gong, M., 2016b. Variant fatty acid-like molecules conjugation, novel approaches for extending the stability of therapeutic peptides. Sci. Rep. 5, 18039.
Marcinkowska-Gapińska, A., Linkowska-Świdzińska, K., Świdziński, T., Surdacka, A., 2018. Rheological parameters of saliva in comparison with taste examination. Biorheology 55, 51–60.
Marinelli, L., Cacciatore, I., Eusepi, P., Di Biase, G., Morroni, G., Cirioni, O., Giacometti, A., Di Stefano, A., 2020. Viscoelastic behaviour of hyaluronic acid formulations containing carvacrol prodrugs with antibacterial properties. Int. J. Pharm. 582, 119306.
Marinelli, L., Dimmito, M.P., Cacciatore, I., Toto, E.C., Di Rienzo, A., Palmerio, F., Puca, V., Di Filippo, E.S., Fulle, S., Di Stefano, A., 2024. Solid lipid nanoparticles for efficient delivery of capsaicin-rich extract: Potential neuroprotective effects in Parkinson's disease. J. Drug Deliv. Sci. Technol. 91, 105097.
Matthew, J., Webber, E., Pashuck, T., 2021. (Macro)molecular self-assembly for hydrogel drug delivery. Adv. Drug Deliv. Rev. 172, 275–295.
Menacho-Melgar, R., Decker, J.S., Hennigan, J.N., Lynch, M.D., 2019. A review of lipidation in the development of advanced protein and peptide therapeutics. J. Control. Release 295, 1–12.
Minelli, A., Conte, C., Cacciatore, I., Cornacchia, C., Pinnen, F., 2012. Molecular mechanism underlying the cerebral effect of Gly-Pro-Glu tripeptide bound to L-dopa in a Parkinson's animal model. Amino Acids 43 (3), 1359–1367.
Mitrovic, J., Richey, G., Kim, S., Guler, M.O., 2023. Peptide hydrogels and nanostructures controlling biological machinery. Langmuir 39, 11935–11945.
Motsoene, F., Abrahamse, H., Kumar, S.S.D., 2023. Multifunctional lipid-based nanoparticles for wound healing and antibacterial applications: a review. Adv. Colloid Interface Sci. 321, 103002.
Myšková, A., Sýkora, D., Kuneš, J., Maletínská, L., 2023. Lipidization as a tool toward peptide therapeutics. Drug Deliv. 30, 2284685.
Nitbani, F.O., Tjitda, P.J.P., Nitti, F., Jumina, J., Detha, A.I.R., 2022. Antimicrobial properties of lauric acid and monolaurin in virgin coconut oil: a review. C.B.E.N. 9, 442–461.
Ong, J.J., Steele, C.M., Duizer, L.M., 2018. Challenges to assumptions regarding oral shear rate during oral processing and swallowing based on sensory testing with thickened liquids. Food Hydrocoll. 84, 173–180.
Pandey, M., Choudhury, H., D/O Segar Singh, S.K., Chetty Annan, N., Bhattamisra, S.K., Gorain, B., Mohd Amin, M.C.I. 2021. Budesonide-loaded pectin/polyacrylamide hydrogel for sustained delivery: fabrication, characterization and in vitro release kinetics. Molecules 26, 2704.
Paramonov, S.E., Jun, H.W., Hartgerink, J.D., 2006. Self-assembly of peptide-amphiphile nanofibers: the roles of hydrogen bonding and amphiphilic packing. J. Am. Chem. Soc. 128, 7291–7298.
Rani, A., De Leon-Rodriguez, L.M., Kavianinia, I., McGillivray, D.J., Williams, D.E., Brimble, M.A., 2016. Synthesis and characterization of mono S-lipidated peptide hydrogels: a platform for the preparation of reactive oxygen species responsive materials. Org. Biomol. Chem. 19, 3665–3677.
Rereddy, S.K., Cao, A.C, Blackwell, B., Poling-Skutvik, R., Arratia, P.E., Mirza, N., 2023. Rheology of saliva in health and disease. Biorheology 59 (1–2), 19–27.
Roy, K., Pandit, G., Chetia, M., Sarkar, A.K., Chowdhuri, S., Bidkar, A.P., Chatterjee, S., 2020. Peptide Hydrogels as platforms for sustained release of antimicrobial and antitumor drugs and proteins. ACS Appl. Bio. Mater. 3, 6251–6262.
Rudyardjo, D.I., Wijayanto, S., 2017. The synthesis and characterization of hydrogel chitosan-alginate with the addition of plasticizer lauric acid for wound dressing application. J. Phys. Conf. Ser. 853, 1742–6598.
Schneider, C.A., Rasband, W.S., Eliceiri, K.W., 2012. NIH image to ImageJ: 25 years of image analysis. Nat. Methods 9, 671–675.
Silva, M.M., Calado, R., Marto, J., Bettencourt, A., Almeida, A.J., Gonçalves, L.M.D., 2017. Chitosan nanoparticles as a mucoadhesive drug delivery system for ocular administration. Mar. Drugs 15, 370.
Stojkov, G., Niyazov, Z., Picchioni, F., Bose, R.K., 2021. Relationship between structure and rheology of hydrogels for various applications. Gels 7, 255.
Tsutsumi, N., Ito, A., Ishigamori, A., Ikeda, M., Izumi, M., Ochi, R., 2021. Synthesis and self-assembly properties of bola-amphiphilic glycosylated lipopeptide-type supramolecular hydrogels showing colour changes along with gel-sol transition. Int. J. Mol. Sci. 22, 1860.
Wang, J., Chin, D., Poon, C., Mancino, V., Pham, J., Li, H., Ho, P.Y., Hallows, K.R., Chung, E.J., 2021. Oral delivery of metformin by chitosan nanoparticles for polycystic kidney disease. J. Control. Release 329, 1198–1209.
Wang, D., Zhang, X., Li, H., Luan, Y., Wei, G., Wang, J., 2019. Anticancer properties of lipidated peptide drug supramolecular self-assemblies with enhanced stability. ACS Appl. Bio. Mater. 2, 5995–6003.
Wu, F., Pang, Y., Liu, J., 2020. Swelling-strengthening hydrogels by embedding with deformable nanobarriers. Nat. Commun. 11, 4502.
Yan, C., Pochan, D.J., 2010. Rheological properties of peptide-based hydrogels for biomedical and other applications. Chem. Soc. Rev. 39, 3528–3540.
Yergoz, F., Hastar, N., Cimenci, C.E., Ozkan, A.D., Tekinay, T., Guler, M.O., Tekinay, A. B., 2017. Heparin mimetic peptide nanofiber gel promotes regeneration of full thickness burn injury. Biomaterials 134, 117–127.
Zhang, L., Bulaj, G., 2012. Converting peptides into drug leads by lipidation. Curr. Med. Chem. 9, 1602–1618.